

Measurement of the differential surface and volume excitation probability of medium energy electrons in solids.

Wolfgang S.M. Werner*

*Institut für Allgemeine Physik, Vienna University of Technology,
Wiedner Hauptstraße 8–10, A 1040 Vienna, Austria*

(Dated: November 17, 2018)

Abstract

A procedure is developed to rigorously decompose experimental loss spectra of medium-energy electrons reflected from solid surfaces into contributions due to surface and volume electronic excitations. This can be achieved by analysis of two spectra acquired under different experimental conditions, e.g. measured at two different energies and/or geometrical configurations. The input parameters of this procedure comprise the elastic scattering cross section and the inelastic mean free path for volume scattering. The (normalized) differential inelastic mean free path as well as the differential surface excitation probability are retrieved by this procedure. Reflection electron energy loss spectroscopy (REELS) data for Si, Cu and Au are subjected to this procedure and the retrieved differential surface and volume excitation probabilities are compared with data from the literature. The results verify the commonly accepted model for medium energy electron transport in solids with unprecedented detail.

PACS numbers: 68.49.Jk, 79.20.-m, 79.60.-i

* werner@iap.tuwien.ac.at,
fax:+43-1-58801-13499, tel:+43-1-58801-13462

1. INTRODUCTION

The susceptibility of a solid to polarize under the influence of an external electromagnetic perturbation governs many physical phenomena taking place at the surface of a solid and therefore determines important technological properties of solid materials. The solid state polarizability is characterized by the frequency and momentum dependent dielectric function $\varepsilon(\omega, q)$. This quantity can be measured by probing a solid surface with elementary particles, e.g. by photon- [1–5] or electron- [6] scattering experiments. A vast number of such experiments has been conducted in the past from which an extensive database of optical data has been established. Furthermore, with the advent of density functional theory beyond the ground state [7], *ab initio* theoretical calculations of optical data have recently become available [8].

Nonetheless there still seems to be a need for experimental work in this field since the available datasets are not always consistent (in particular in the range between the visible and vacuum-ultra-violet (VUV)-part of the optical spectrum) which complicates comparison with theoretical results. One commonly accepted reason for the inconsistency of the available datasets is that the early experiments were not always conducted under ultra-high-vacuum (UHV) conditions. However, there also exist inherent problems with the conventional methods to measure optical data. In photon scattering experiments, it is difficult to reach the UV-part of the optical spectrum and, moreover, it is not straightforward to use such experiments to study structures on the sub nanometer scale since photons are hard to focus. The latter deficiency can be overcome by employing transmission electron energy loss measurements, which are moreover dominated by the dielectric response in the UV-regime, but even nowadays these experiments are still not routinely conducted under UHV-conditions and, moreover, specimen preparation puts quite a strict limit on the types of nanostructures that can be investigated with this technique.

Reflection electron energy loss spectroscopy (REELS) measurements have the potential to bridge this gap. Like any charged particle scattering experiment, such loss spectra are dominated by the UV-response, the experimental procedure is extremely simple, it is routinely carried out under UHV conditions and can nowadays be performed with sub-nm lateral resolution on a large number of instruments on a specimen prepared in an arbitrary way.

Owing to the energy dependence of the quasi-elastic backscattering coefficient that de-

creases rapidly above several keV for any material [9], such experiments need to be carried out in the medium energy range (several hundred to several thousands of an eV). Unfortunately this severely complicates quantitative interpretation of REELS spectra which are obscured in this energy range by the occurrence of multiple surface and volume excitations. Furthermore, the particles are multiple elastically scattered and the elastic scattering cross section exhibits a pronounced energy and angular dependence. Therefore, the interaction of the probing particle with the solid is governed by multiple scattering processes of different types and is consequently very complex. This is the reason why earlier proposed procedures to extract optical data from REELS measurements have not led to satisfactory results [10–12]. Since, on the other hand, such experiments have a great potential for the measurement of optical data, as outlined above, an attempt to resolve the problems addressed above seems worthwhile. This requires, in a first step, the development of a procedure to extract the distribution of energy losses in an individual bulk and surface excitation from an experimental spectrum, which is dominated by multiple scattering processes of different types. In a further step these loss distributions need to be converted to optical data.

In the present work, the first step of this ambitious programme is addressed. The elementary interaction characteristics are reviewed and it is shown that in Fourier space, the loss spectrum can be expressed as a bivariate power series in the bulk and surface scattering distributions in an individual collision. An algorithm to reverse this bivariate power series using a pair of loss spectra taken under different experimental conditions is developed. The procedure is successfully applied to experimental loss spectra of 20 elemental solids. The resulting distribution of energy losses is presented for Si, Cu and Au and compared with theoretical results based on optical data from various sources in the literature.

2. THEORETICAL

2.1. Elementary interaction characteristics

The degrees of freedom of a medium energy electron traversing a solid are subject to fluctuations brought about by the strong interaction of the probing electron with the ionic and electronic subsystem of the solid. Owing to the large mass difference between the incoming electron and the ionic subsystem on one hand and the similarity of the mass of the

probing electron and the electronic subsystem on the other hand, large momentum transfers are accompanied by small energy losses and vice versa [9]. Therefore the distinction between *elastic* and *inelastic* scattering is a meaningful one for medium energy electrons.

For non-crystalline solids, where diffraction effects (coherent scattering) are insignificant [13], the interaction with the ionic subsystem is adequately described [9] in terms of an atomic cross section for elastic scattering $d\sigma_e(\Omega)/d\Omega$, that can be established *ab initio* on the basis of a screened Coulomb potential for free atoms [14]. The solid is modelled as a random array of scattering centres, and the mean distance between successive elastic deflection processes, the so-called elastic mean free path λ_e is the reciprocal of the differential elastic cross section integrated over the unit sphere multiplied with the density N_a of scattering centres [9].

The inelastic interaction is commonly conceived as a deceleration of the incoming electron by a polarization field set up by it inside the solid. The susceptibility of the solid to the external perturbation is given in terms of its frequency (ω) and momentum (q) dependent dielectric function $\varepsilon(\omega, q)$. Extensive data for the dielectric function of solids are available in the literature for zero momentum transfer [1–5]. The dielectric function for arbitrary momentum transfers can be obtained by fitting a Drude–Lindhard type expansion to such optical data (see e.g., Ref. [15]), invoking an appropriate dispersion relation to extrapolate the optical loss function onto the (ω, q) -plane.

In electron reflection measurements it is obviously not possible to discriminate individual momentum transfers in an inelastic process. Rather, reflection energy loss spectra represent an average over all possible momentum transfers, in contrast to transmission experiments, which are conducted in the single-scattering regime and allow to discriminate the momentum transfer by means of angle resolved experiments [6]. Therefore, for REELS, the basic physical quantity governing inelastic scattering deep inside the solid is the differential inverse inelastic mean free path (DIIMFP) $W_b(T)$, i.e. the distribution of energy losses $T = \hbar\omega$ per unit pathlength in an individual collision. It is related to the dielectric function $\varepsilon(\omega, q)$ of the solid via the well known formula [16]:

$$W_b(\omega) = \frac{1}{\pi E} \int_{q_-}^{q_+} \mathcal{I}m \left\{ \frac{-1}{\varepsilon(\omega, q)} \right\} \frac{dq}{q} \quad (1)$$

where the subscript "b" indicates bulk inelastic scattering deep inside the solid, E is the energy of the incoming electron and q is the momentum transfer which, for parabolic bands,

is confined by q_- and q_+ given by:

$$q_{\pm} = \sqrt{2E} \pm \sqrt{2(E - \omega)} \quad (2)$$

In the above expressions as well as in the remainder of this section, atomic units are used, unless indicated otherwise. The average path length between successive inelastic collisions in the bulk of the solid, the so-called inelastic mean free path λ_i (IMFP) is a quantity of paramount importance for electron spectroscopy and is the reciprocal of the DIIMFP integrated over all possible energy losses. The differential inverse mean free path normalized to unity area, that will be denoted by $w_b(T)$ in the following, is related to the unnormalized DIIMFP via $w_b(T) = \lambda_i W_b(T)$.

In the vicinity of the surface, both in vacuum and inside the solid, additional modes of the inelastic interaction, so-called surface excitations, occur, as required by the boundary conditions of Maxwell's equations. Several models to describe surface excitations have been put forward in the past [11, 15, 17–24]. The resonance frequency ω_s of these surface modes (indicated by the subscript "s" in the following) is slightly lower than for volume excitations. The distribution of surface energy losses decays faster with the energy loss than for volume losses: while the distribution of volume losses tails off slowly towards the maximum energy loss given by the energy E of the probing electron, the typical energy loss for which the distribution of surface losses drops below a relevant value is much smaller than for bulk losses, usually it is less than 50 eV. Furthermore, surface excitations exhibit a pronounced depth dependence, decaying rapidly with the depth from the surface both inside the solid and in vacuum. The decay length is of the order of $v/\omega_s \sim 5 \text{ \AA}$, where v is the speed of the electron. Since this decay length is of the order of, or smaller than, the elastic mean free path λ_e , the part of an electrons trajectory passing through the surface scattering zone is approximately rectilinear, at least inasmuch as in vacuum the dynamic interaction of the electron with its image charge can be neglected [22]. Therefore it makes sense to use the differential surface excitation probability $W_s(E, \theta)$ (DSEP) as basic physical quantity to describe surface excitations, i.e. the integral of the differential mean free path over the surface scattering zone, where θ is the polar angle of surface crossing. Tung and coworkers [15] give the following expression for the DSEP:

$$W_s(\omega, \theta, E) = P_s^+(\omega, \theta, E) + P_s^-(\omega, \theta, E) \quad (3)$$

where the quantity $P_s^\pm(\omega, \theta, E)$ is defined as

$$P_s^\pm(\omega, \theta, E) = \frac{1}{\pi E \cos \theta} \int_{q_-}^{q_+} \frac{|q_s^\pm| dq}{q^3} \text{Im} \left[\frac{(\varepsilon(\omega, q) - 1)^2}{\varepsilon(\omega, q)(\varepsilon(\omega, q) + 1)} \right] \quad (4)$$

and

$$q_s^\pm = \left[q^2 - \left(\frac{\omega + q^2/2}{\sqrt{2E}} \right)^2 \right]^{1/2} \cos \theta \pm \left(\frac{\omega + q^2/2}{\sqrt{2E}} \right) \sin \theta \quad (5)$$

The total surface excitation probability $\langle n_s(\theta, E) \rangle$ is obtained from expression (3) by integrating over the energy loss. Note that this (dimensionless) quantity, that will be referred to as (total) surface excitation probability (SEP) below, is equal to the average number of surface excitations in a single surface crossing. The normalized differential surface excitation probability is therefore given by $w_s(T, \theta) = W_s(T, \theta) / \langle n_s(\theta, E) \rangle$.

To avoid confusion, it is noted that although the same symbol ("W" in W_b and W_s) is used to denote the distribution of energy losses in a surface and bulk excitation, the physical meaning of these quantities is quite different. While the DIIMFP is the volume scattering probability per unit path length and energy, the DSEP represents the surface excitation probability per unit energy, since this quantity is obtained by integrating over the path the electron takes through the surface scattering zone[15]. The normalized distribution of energy losses $w_b(T)$ and $w_s(T)$ are physically equivalent quantities and both have the dimension of reciprocal energy, which is the reason why the same symbol is chosen for these quantities (see the next section).

Examples for the DIIMFP and DSEP for Si and Au are given in Figure 1. The DIIMFP is shown for two energies (1000 and 3000 eV), while the DSEP is given for 1000 eV for two different surface crossing angles of 0° and 70° . It is seen that for the considered energy loss range, being significantly smaller than the probing energy, the shape of the DIIMFP hardly depends on the energy, or, in other words, that the *normalized* distribution of energy losses is independent of the incoming energy $w_b(T, E) \simeq w_b(T)$ to a good approximation. The same holds for the DSEP (not shown). On the other hand, the angular dependence of the *normalized* DSEP is seen to be very weak as well, $w_s(T, E, \theta) \simeq w_s(T)$. Of course the *total* surface excitation probability $\langle n_s(E, \theta) \rangle$ exhibits a pronounced angular and energy dependence, while the energy dependence of the IMFP, $\lambda_i(E)$, that governs the total bulk scattering probability, is appreciable as well.

Comparison of these quantities for Si and Au clearly reveals the pronounced difference of

the electronic structure of these materials: while the inelastic interaction in Si is governed by the collective plasmon-modes of the weakly bound solid state electrons, inter- and intraband transitions determine the shape of the energy loss distributions of Au.

Another noteworthy feature in this figure is the negative excursion of the DSEP, being very pronounced for Si, while it is much weaker for Au, but still clearly distinguishable. This is a consequence of the coupling between the bulk and surface modes, that are orthogonal, and is commonly referred to as *begrenzungseffect* after the German word for boundary[17]. In other words, in the presence of the surface, the intensity of the volume modes is decreased owing to the depolarization of the surface charge by the surface modes. This is clearly seen in the case of Si where the negative excursion peaks exactly at the energy loss corresponding to a volume plasmon loss. This means that the DSEP in fact consists of two terms: the pure surface term, which is positive, and the *begrenzungs-* or coupling term, which is negative. It also makes it clear that surface and bulk excitations are different modes of the same phenomenon and that the distinction between these two types of inelastic scattering is essentially artificial. Nonetheless, for practical purposes it is useful to make this distinction in the sense that volume excitations are considered as those loss processes that occur in an infinite boundless medium, while surface excitations are defined as all changes in the loss probability due to the presence of a boundary. Thus, in accordance with this definition, the DSEP is in fact a difference of two loss probabilities, the pure and the coupling term and a negative excursion in the DSEP is observed whenever the latter exceeds the former.

In conclusion of this section, it is noted that several semi-empirical formulae have been published to estimate the IMFP [25] and the SEP [26]. The latter quantity is given in terms of a material parameter a_s , the so-called surface excitation parameter, by the formula:

$$\langle n_s(E, \theta) \rangle = \frac{1}{a_s \sqrt{E} \cos \theta + 1} \quad (6)$$

The quantity a_s is given for a large number of elemental solids in Ref. [26] in units of the free electron value $a_{NFE} = \sqrt{8a_0/\pi^2 e^2} = 0.173 eV^{-1/2}$, where $e^2 = 14.4 eV \text{\AA}$ is the elementary charge squared and $a_0 = 0.52 \text{\AA}$ is the Bohr radius. An empirical relationship between the surface excitation parameter a_s and the generalized plasmon energy was also derived, allowing one to estimate the extent of surface excitations for an arbitrary material.

2.2. Multiple scattering

The energy and direction of motion of a charged particle travelling through a solid is changed repeatedly by multiple scattering processes. For non-crystalline materials, where coherent scattering can be neglected [13] the fluctuations after multiple scattering can be expressed in terms of the fluctuation distributions in a single collision, that were introduced in the previous section, by solving a linearized Boltzmann-type kinetic equation [27]. The Green's function of this problem can be expressed in terms of the $(n-1)$ -fold selfconvolution of the single scattering fluctuation distributions weighted with the collision statistics, i.e. the number of times n a given scattering process occurs for the considered boundary conditions [Eq. (12) in Ref. [27]]. The resulting spectrum, or yield, $Y(E)$ (for one type of inelastic scattering) is then found by superposition:

$$Y(E) = \sum_{n=0}^{\infty} A_n \Gamma_n(T) \otimes f_0(E + T) \quad (7)$$

Here $f_0(E)$ is the energy distribution at the source and the symbol " \otimes " denotes a convolution over the energy loss T . The quantities $\Gamma_n(T)$ represent the (normalized) distribution of energy losses after n collisions and are given by the $(n-1)$ -fold selfconvolution of the single scattering fluctuation distribution $w(T)$ [27]:

$$\begin{aligned} \Gamma_{n=0}(T) &= \delta(T) \\ \Gamma_n(T) &= \Gamma_{n-1}(T') \otimes w(T - T') \end{aligned} \quad (8)$$

where $w(T)$ is the *normalized* distribution of energy losses in an individual collision.

The partial intensities A_n represent the number of electrons that arrive in the detector after being n -fold inelastically scattered in the solid and are given by an integral over all possible lengths of the paths s taken by the particle in the solid:

$$A_n = \int_0^{\infty} W_n(s) Q(s) ds \quad (9)$$

Here $Q(s)$ is the distribution of pathlengths and $W_n(s)$ is the stochastic process for multiple scattering, which, in the quasielastic regime, is given by [28]:

$$W_n(s) = \left(\frac{s}{\lambda_i} \right)^n \frac{e^{-s/\lambda_i}}{n!} \quad (10)$$

In a REELS experiment, the incoming electron experiences surface excitations on the way into the solid, is multiple scattered in the bulk and again suffers a surface electronic energy loss when crossing the solid–vacuum boundary on its way out of the solid. In the following, the ingoing and outgoing part of the trajectory will be denoted by the superscripts "i" and "o", respectively. When interference effects between the different types of inelastic scattering can be neglected [9], the total energy fluctuation distribution for all types of scattering is given by a convolution of the individual fluctuation distributions and Equation (7) may be generalized as follows:

$$Y(E) = \sum_{n_b=0}^{\infty} \sum_{n_s^i=0}^{\infty} \sum_{n_s^o=0}^{\infty} A_{n_b, n_s^i, n_s^o} \Gamma_{n_b}(T) \otimes \Gamma_{n_s^i}(T') \otimes \Gamma_{n_s^o}(T'') \otimes f_0(E + T + T' + T'') \quad (11)$$

As mentioned before, the width of the surface scattering zone v/ω_s is smaller than, or of the order of, the elastic mean free path λ_e . In this case the electrons path in the surface scattering zone is rectilinear to a good approximation. A most beneficial consequence of this fact is that the partial intensities for the three types of scattering are uncorrelated [29]:

$$A_{n_b, n_s^i, n_s^o} = A_{n_b} \times A_{n_s^i} \times A_{n_s^o} \quad (12)$$

Although (small) effects of deflections in the surface scattering zone have been experimentally observed for a rather pathological case [30], implying that Eqns. (12) (and (13) below) are not strictly true, this approach nonetheless has proven to constitute an effective approximation [29–32].

Since there exists a unique straight line path connecting any two points in space, the part of the pathlength distribution relevant for surface excitations resembles a δ –function, $Q_s(s) \approx \delta(s - v/\omega_s \mu_i)$ when the passage through the surface scattering zone is approximately rectilinear. In this case Equation (9) can readily be integrated giving:

$$A_{n_s^i}(\mu_i) = \frac{\langle n_s^i(\mu_i) \rangle^{n_s^i}}{n_s^i!} e^{-\langle n_s^i(\mu_i) \rangle} \quad (13)$$

Where the shorthand notation $\mu_i = \cos \theta_i$ was used to indicate the incident polar direction of surface crossing. This reveals that the average number of surface excitations may alternatively be expressed as:

$$\langle n_s^i(\mu_i) \rangle \approx \frac{v}{\omega_s \lambda_i^{s,i} \mu_i}, \quad (14)$$

where $\lambda_i^{s,i}$ is the effective inelastic mean free path for surface scattering along the incoming part of the trajectory. Analogous expressions hold for the outgoing partial intensities.

For bulk inelastic scattering the situation is more complicated. The distribution of path-lengths depends in a complex manner on the incident and outgoing angle and the energy of the particle [9, 30, 31, 33]. Therefore the partial intensities for bulk scattering, A_{n_b} , are most conveniently established by calculating the pathlength distribution by some numerical procedure, e.g., a Monte Carlo calculation [9, 34], and using Equation (9).

Examples for the bulk partial intensities are given in Figure 2 for electrons of various energies reflected from a Si and a Au surface for normal incidence and for an off-normal emission angle of 60° , corresponding to the geometrical configuration used throughout this work. The sequence of partial intensities is seen to be qualitatively different for the two considered materials and also for the different energies considered. This is a well known effect [30, 33, 34] that is caused by the relative strength of elastic and inelastic scattering for a given geometrical configuration, being governed by the complex energy and angular dependence of the elastic scattering cross section.

To simplify Equation (11), the reduced spectrum $y(E)$ is introduced. This is the spectrum divided by the area of the elastic peak. The latter is per definition given by the zero order partial intensity $A_{n_b=0, n_s^i=0, n_s^o=0}$. It will furthermore be assumed that the width of energy distribution at the source (i.e. the thermal spread in the electron gun) is negligible compared to the width of any feature in the relevant differential mean free paths, implying that the source energy distribution can be replaced by a δ -function, $f_0(E) = \delta(E - E_0)$ where E_0 is the source energy. For the following manipulations, it is convenient to consider the Fourier transform of the spectrum, since, by virtue of the convolution theorem, this quantity can be written as a power series in the respective mean free paths [cf. Equation (8)]. Below, any quantity in Fourier space will be indicated by a tilde sign ("~"). The Fourier transform of the reduced spectrum is given by:

$$\tilde{y} = \sum_{n_b=0}^{\infty} \sum_{n_s^i=0}^{\infty} \sum_{n_s^o=0}^{n_s^i} \alpha_{n_b, n_s^o, n_s^i - n_s^o} \tilde{w}_b^{n_b} \tilde{w}_{s,i}^{n_s^o} \tilde{w}_{s,o}^{n_s^i - n_s^o} \quad (15)$$

where the reduced partial intensities $\alpha_{n_b, n_s^i, n_s^o} = A_{n_b, n_s^i, n_s^o} / A_{n_b=0, n_s^i=0, n_s^o=0}$ were introduced. Note that the order of the summation in Equation (15) was also changed. Using expression (12) and (13) and the binomial theorem, one finds:

$$\tilde{y} = \sum_{n_b=0}^{\infty} \alpha_{n_b} \tilde{w}_b^{n_b} \sum_{n_s=0}^{\infty} \frac{(\langle n_s^i \rangle \tilde{w}_{s,i} + \langle n_s^o \rangle \tilde{w}_{s,o})^{n_s}}{n_s!} \quad (16)$$

where $n_s = n_s^i + n_s^o$. Since the results in Figure 1 clearly show that the normalized DSEP only depends weakly on the surface crossing angle, it is reasonable to put $w_{s,i}(T) \approx w_{s,o}(T) \equiv w_s(T)$, in this way combining the effects of surface excitations along the in- and outgoing part of the trajectory. Going back to real space, this gives:

$$y(E) = \sum_{n_b=0}^{\infty} \sum_{n_s=0}^{\infty} \alpha_{n_b} \alpha_{n_s} \Gamma_{n_b}(T) \otimes \Gamma_{n_s}(T') \otimes \delta(E - E_0 + T + T') \quad (17)$$

where α_{n_s} are the reduced partial intensities for surface scattering

$$\alpha_{n_s} = \frac{A_{n_s}}{A_{n_s=0}} = \frac{\langle n_s \rangle^{n_s}}{n_s!} \quad (18)$$

and with $\langle n_s \rangle = \langle n_s^i(\mu_i) \rangle + \langle n_s^o(\mu_o) \rangle$.

Finally, the elastic peak is removed from the spectrum and the energy scale is converted to an energy loss scale giving the reduced *loss* spectrum $y_L(T)$ as:

$$y_L(T) = \sum_{n_b=0}^{\infty} \sum_{n_s=0}^{\infty} \alpha_{n_b, n_s} \Gamma_{n_b}(T') \otimes \Gamma_{n_s}(T - T') \quad (19)$$

with $\alpha_{n_b=0, n_s=0} = 0$. This form of the loss spectrum is used in the further analysis.

2.3. Decomposition of REELS spectra

It is the objective of the present work to extract the DIIMFP and DSEP from experimental loss spectra. Recognizing Equation (19) as a bivariate power series (in \tilde{w}_b and \tilde{w}_s) in Fourier space, it is immediately obvious that this equation has no unique solution. However, when *two* loss spectra with different partial intensities

$$\begin{aligned} \tilde{y}_{L,1} &= \sum_{n_s=0}^{\infty} \sum_{n_b=0}^{\infty} \alpha_{n_s, n_b} \tilde{w}_b^{n_b} \tilde{w}_s^{n_s} \\ \tilde{y}_{L,2} &= \sum_{n_s=0}^{\infty} \sum_{n_b=0}^{\infty} \beta_{n_s, n_b} \tilde{w}_b^{n_b} \tilde{w}_s^{n_s}, \end{aligned} \quad (20)$$

with $\alpha_{0,0} = \beta_{0,0} = 0$, are measured, reversion of the bivariate power series becomes possible. Experimentally, this implies that two loss spectra need to be acquired at different energies and/or geometrical configurations. From the theoretical point of view, we need to make the assumption, in this case, that the normalized DIIMFP and DSEP are independent of the surface crossing angle and/or the energy to a good approximation (cf. Figure 1).

Formally, the reversion of this bivariate power series is effected by the expansion:

$$\begin{aligned}\tilde{w}_b &= \sum_{p=0}^{\infty} \sum_{q=0}^{\infty} u_{p,q}^b \tilde{y}_{L,1}^p \tilde{y}_{L,2}^q \\ \tilde{w}_s &= \sum_{p=0}^{\infty} \sum_{q=0}^{\infty} u_{p,q}^s \tilde{y}_{L,1}^p \tilde{y}_{L,2}^q\end{aligned}\tag{21}$$

with $u_{0,0}^b = u_{0,0}^s = 0$. This can be seen by substituting Equation (20) back into Equation (21) and equating coefficients of equal powers of \tilde{w}_b and \tilde{w}_s . This gives the equations for the unknown coefficients $u_{p,q}^b$ and $u_{p,q}^s$.

In doing so, one is faced with the problem of evaluating the p -th power of $\tilde{y}_{L,1}$ times the q -th power of $\tilde{y}_{L,2}$ that can be expressed as:

$$\tilde{y}_{L,1}^p \tilde{y}_{L,2}^q = \sum_{n_s=0}^{\infty} \sum_{n_b=0}^{\infty} \gamma_{p,q,n_b,n_s} \tilde{w}_b^{n_b} \tilde{w}_s^{n_s}\tag{22}$$

The components of the tensor γ_{p,q,n_b,n_s} are found to be given by:

$$\gamma_{p,q,n_b,n_s} = (\alpha_p, \beta_q)_{(n_b,n_s)}^{(p+q)}\tag{23}$$

These components are equal to the sum of all possible terms with p factors in $\alpha_{k,l}$ and q factors in $\beta_{m,n}$, whose indices "add up" to the target index combination $(n_s, n_b) = (k + m, l + n)$. For example:

$$\begin{aligned}(\alpha_2)_{(2,1)}^2 &= \alpha_{1,0}\alpha_{1,1} + \alpha_{0,1}\alpha_{2,0} + \alpha_{1,1}\alpha_{1,0} + \alpha_{2,0}\alpha_{0,1} \\ (\alpha_1, \beta_2)_{(1,2)}^3 &= \alpha_{0,1}\beta_{0,1}\beta_{1,0} + \alpha_{0,1}\beta_{1,0}\beta_{0,1} + \alpha_{1,0}\beta_{0,1}\beta_{0,1}\end{aligned}\tag{24}$$

Obviously, one has

$$\gamma_{p,q,n_b,n_s} = 0 \quad \text{for all } p + q > n_s + n_b\tag{25}$$

since the target index combination (n_s, n_b) can only be produced by a number of factors less than or equal to $(n_s + n_b)$ when $\alpha_{0,0} = \beta_{0,0} = 0$ [see Equation (20)]. Furthermore, one has:

$$\begin{aligned}\gamma_{n_b,n_s,1,0} &= \alpha_{n_b,n_s} \\ \gamma_{n_b,n_s,0,1} &= \beta_{n_b,n_s}\end{aligned}\tag{26}$$

Based on these guidelines, the tensor γ_{p,q,n_b,n_s} can readily be established by means of a recursive algorithm for any sequence of partial intensities α_{n_b,n_s} and β_{n_b,n_s} .

Inserting Equation (20) into Equation (21) and equating coefficients, one finds a set of two equations with two unknowns for the first order bulk coefficients:

$$\begin{aligned} 1 &= \sum_{p=0}^{\infty} \sum_{q=0}^{\infty} u_{p,q}^b \gamma_{p,q,1,0} = u_{0,1} \beta_{1,0} + u_{1,0} \alpha_{1,0} \\ 0 &= \sum_{p=0}^{\infty} \sum_{q=0}^{\infty} u_{p,q}^b \gamma_{p,q,0,1} = u_{0,1} \beta_{0,1} + u_{1,0} \alpha_{0,1} \end{aligned} \quad (27)$$

The solution is:

$$\begin{aligned} u_{1,0}^b &= \frac{\beta_{0,1}}{\beta_{0,1} \alpha_{1,0} - \beta_{1,0} \alpha_{0,1}} \\ u_{0,1}^b &= \frac{\alpha_{0,1}}{\alpha_{0,1} \beta_{1,0} - \alpha_{1,0} \beta_{0,1}} \end{aligned} \quad (28)$$

Similarly, for the first order surface coefficients one finds:

$$\begin{aligned} u_{1,0}^s &= \frac{\beta_{1,0}}{\beta_{1,0} \alpha_{0,1} - \beta_{0,1} \alpha_{1,0}} \\ u_{0,1}^s &= \frac{\alpha_{1,0}}{\alpha_{1,0} \beta_{0,1} - \alpha_{0,1} \beta_{1,0}} \end{aligned} \quad (29)$$

The equation determining the higher order ($p + q > 1$) coefficients

$$0 = \sum_{p=0}^{\infty} \sum_{q=0}^{\infty} u_{p,q} \gamma_{p,q,n_b,n_s} \quad (30)$$

can be split into two parts by using property (25), changing the order of the summation and writing:

$$0 = \sum_{p=0}^{n_s+n_b-1} \sum_{q=0}^p u_{q,p-q} \gamma_{q,p-q,n_b,n_s} + \sum_{p=0}^{n_s+n_b} u_{p,n_s+n_b-p} \gamma_{p,n_b+n_s-p,n_b,n_s} \quad (31)$$

The first term represents a $(n_s + n_b + 1)$ -dimensional vector containing the coefficients $u_{p < n_b, q < n_s}$, which have been established during the previous step of the algorithm. The latter term is the product of a square matrix with the same dimension and the unknown vector $(u_{0,n_b+n_s}, u_{1,n_b+n_s-1}, u_{2,n_b+n_s-2}, \dots, u_{n_b+n_s,0})$. Thus, for each value of $n_b + n_s$, the corresponding coefficients are obtained by solution of a system of $n_b + n_s + 1$ linear equations with as many unknowns. Consecutively performing this procedure for values of the total scattering order $n_b + n_s = 1, 2, \dots, n_{max}$, where n_{max} is the collision order where convergence of the series Equation (21) is attained, leads to the desired coefficient matrices $u_{p,q}^b$ and $u_{p,q}^s$. Note that Eqns. (30) and (31) are identical for the surface and bulk coefficients, only the calculation for the first order term is different [see Eqns. (28) and (29)]

Finally, having established the bulk and surface expansion coefficients, the Fourier back-transform of Equation (21) gives:

$$\begin{aligned} w_b(T) &= \sum_{p=0}^{\infty} \sum_{q=0}^{\infty} u_{p,q}^b y_{L,1}^{(p)}(T') \otimes y_{L,2}^{(q)}(T - T') \\ w_s(T) &= \sum_{p=0}^{\infty} \sum_{q=0}^{\infty} u_{p,q}^s y_{L,1}^{(p)}(T') \otimes y_{L,2}^{(q)}(T - T') \end{aligned} \quad (32)$$

where $y_{L,1}^{(p)}$ and $y_{L,2}^{(q)}$ denote the $(p - 1)$ -fold selfconvolution of $y_{L,1}$ and the $(q - 1)$ -fold selfconvolution of $y_{L,2}$, respectively.

3. RESULTS AND DISCUSSION

The procedure outlined above was implemented and applied to simulated data, to test its performance in terms of numerical stability and accuracy. Subsequently it was applied to experimental REELS spectra, to gain information on the dielectric response of several solids to incoming electrons. In all cases, the pair of spectra considered was a set of two REELS spectra taken at different energies, but for the same geometrical configuration.

Calculation of the tensor γ_{p,q,n_b,n_s} was performed using a simple recursive algorithm (about 20 lines of code), following the guidelines given in the previous section. While computation of the first few orders ($p + q \leq 7$) takes several seconds on a modern PC, the 8-th order alone takes 10 seconds, the 9th order 10 ten minutes, the 10th order takes several hours and the 11th order several weeks. Although faster algorithms for reversion of multivariate power series are available [35–37], these are quite complex and were not considered since convergence of the proposed algorithm is typically attained for $n_{max} \leq 7$ for energy loss ranges extending up to 100 eV.

The convergence of the algorithm can be assessed in a simple way by using the retrieved DSEP and DIIMFP to simulate the loss spectra and compare these with the original loss spectra from which these quantities were retrieved. For the energy range for which the procedure has attained convergence, these simulated spectra are *exactly* identical to the input spectra, while for higher energies, corresponding to scattering orders beyond the value of n_{max} , they diverge rapidly. In this way the required value of n_{max} can easily be determined for a specific application. For the results shown in the present work, the maximum energy loss considered was 100 eV and the procedure converged for $n_{max} = 5 - 7$.

It was found that the outlined algorithm is very robust when a reasonable choice for the difference of the partial intensities of the two input spectra is made. The stability of the procedure is governed by the quantity $\Delta = |\beta_{1,0}\alpha_{0,1} - \beta_{0,1}\alpha_{1,0}|$ which should not be too much smaller than unity $\Delta \gtrsim 0.1$ when the procedure is applied to experimental data. On the other hand the difference in energy/emission angle should not be too large since then the difference of the normalized DIIMFP/DSEP for the different experimental conditions becomes more pronounced. This implies that one should select that combination of energies for which this criterion is optimally fulfilled (see Figure 2).

Spectra were simulated by calculation of the pathlength distribution using a Monte Carlo algorithm [34] and using Equation (9) to calculate the bulk partial intensities. The inelastic mean free path was derived from the TPP-2M formula [25], and elastic cross sections were calculated with the computer code of Ref.[38] for a Thomas–Fermi–Dirac potential [39]. The surface partial intensities were obtained from Equation (13), using the values for the SEP given in Ref. [26]. The DSEP and DIIMFP were established by means of Eqns. (1) and (4) using the Drude-Lindhard parameters for the dielectric function in Ref. [15].

Three different types of simulated spectra were analyzed before the procedure was applied to experimental data, in order to assess the influence of several assumptions that are made in this procedure on the outcome of a retrieval operation: (I.) loss spectra that were simulated for an elastic peak modelled by a true δ -function and using identical normalized DIIMFPs and DSEP for both energies/geometries of the spectrum pair; (II.) loss spectra that were simulated taking into account the energy/angular dependence of the normalized loss distributions using an infinitely sharp elastic peak; and (III.) loss spectra with different DIIMFP and DSEP at the considered energies/geometries and using an elastic peak with a finite width. These different types of model calculations will be referred to below by their roman numeral indicated above.

The type I model calculations always returned the exact model DIIMFP and DSEP (within the numerical precision of the PC), even when a significant amount of noise was added to the model spectra. When the energy dependence of the DIIMFP and DSEP is accounted for in the simulation (type II model calculations), minor deviations were observed, of the order of the deviations seen for different energies/angles shown in Figure 1. These deviations were more pronounced –but still minor– for sharply peaked loss distributions (e.g., for Si). When a finite width of the elastic peak was used (type III model calculations),

the retrieved loss distributions become smoother. Results of type III model calculations are shown and discussed below where the retrieval results using experimental data are presented.

The procedure used to acquire the experimental data has been described in detail before [34]. REELS data were taken for 20 elemental solids (Ag, Al, Au, Be, Bi, C, Co, Cu, Fe, Ge, Mo, Ni, Pd, Pt, Si, Ta, Te, Ti, V, W) in the energy range between 300 and 3400 eV for normal incidence and an off-normal emission angle of 60° , using a hemispherical analyzer operated in the constant analyzer energy mode giving a width of the elastic peak of 0.7 eV. Count rates in the elastic peaks were kept well below the saturation count rate of the channeltrons and a dead time correction was applied to the data. For each material the optimum energy combination for the retrieval procedure of two loss spectra was determined by inspection of the partial intensities. For most materials the optimum energy combination was (1000-3000 eV).

Figure 3-5 show the results for Si, Cu and Au. In (a.) the experimental loss spectra used as input are represented by the noisy curves. These loss spectra were obtained from the REELS spectra by fitting the elastic peak to a Gaussian. Subsequently, the experimental data were divided by the area under this curve, the fitted peak was subtracted from them and the energy scale was converted to an energy loss scale. Finally, the measured spectrum $S_L(T)$ [in counts per channel] was converted to experimental yield $y_L(T)$ [in reciprocal eV], corresponding to Equation (19), by division by the channel width ΔE .

The smooth curves in (a.) are the simulated spectra for an elastic peak width matching that of the experimental data and with the energy dependence of the normalized loss distributions taken into account (type III model calculations). In (b.) the retrieved normalized DIIMFP (open circles) is compared with the theoretical DIIMFP [Equation (1), solid curves] and with the DIIMFP retrieved from the simulated spectra (type III model calculations, dotted curve). In (c.) the retrieved normalized DSEP is compared with theory [Equation (4), solid curves] and the result based on simulated spectra (type III model calculations, dotted curves). The results in (b.) and (c.) are presented as returned by the decomposition algorithm, and were not scaled in any way. Finally, the DIIMFP and DSEP retrieved from the experimental data were used to calculate another set of model spectra which are compared in (a.) with the experimental data, but are impossible to distinguish from the latter since these model data *exactly* coincide with the experimental data since Equation (32) and Equation (20) are each others *exact* inverse for the energy loss range

where convergence has been attained.

The raw loss spectra for Si shown in Figure 3a are seen to be quite similar for 1000 and 3000 eV. Close inspection of the loss features for the fourth and fifth order plasmon reveals that the data for 1000 eV decrease slightly faster with increasing energy loss than for 3000 eV, in full accordance with the partial intensities for these energies, shown in Figure 2a. However, the main difference between the two spectra is the relative intensity of the first surface plasmon, being clearly lower for 3000 eV. The main difference between the experimental data and the simulated REELS spectra is the fact that the experimental plasmon peaks are broader than the simulated ones, and in consequence the intensity at higher loss energies is lower than for the simulated data.

The retrieved bulk loss distribution (open circles in Figure 3b) agrees fairly well with the result predicted by theory (solid curve), but significant deviations are observed as a shoulder at around 12 eV and a spurious peak at about twice the volume plasmon energy. However, these features are also present in the loss distribution retrieved from the simulated spectra (type III model calculations, dotted lines). Furthermore, the feature at ~ 12 eV exactly coincides with the peak in the difference distribution ΔDSEP in Figure 1a. The ΔDIIMFP difference distribution has a peak in the vicinity of bulk plasmon energy implying that the theoretical sequence of partial intensities no longer matches those required for the retrieval (since the area under the normalized DIIMFP is different). In consequence, the elimination of the second bulk plasmon is not complete, exactly as observed in the data at about 32 eV. It can therefore be concluded that the deviations between the theoretical loss distributions –for Si, with quite sharp peaked loss features– and those retrieved from experimental data are mainly a consequence of the energy dependence of the *shape* of the DIIMFP and the angular dependence of the *shape* of DSEP (see Figure 1), which is ignored by Equation (32).

For the differential surface excitation probability, a similar behaviour is seen: near 32 eV, a second negative excursion, apart from the theoretically expected *begrenzungs*-effect at ~ 16 eV, can be seen. Again this feature is also present in the type III model data and can thus be attributed to the energy dependence of the shape of the DIIMFP and DSEP. The *begrenzungs*-effect itself is quite nicely reproduced by the experimental loss distributions. The only deviation from theory that cannot be explained by the assumption that the shape of the DIIMFP and DSEP do not depend on the energy and surface crossing angle are the features below ~ 10 eV, being significantly higher than the type III model calculations and

rendering the overall shape of the DSEP broader than theoretically expected. This explains the differences between the model data and experiment in Figure 3a. Such deviations were observed before [29] but a clear explanation has not been proposed. We note, however, that the physical model for electron reflection discussed in the present paper completely disregards direct creation of electron-hole pairs as a result of the impact of the primary electrons on the solid.

The differences between the simulated and experimental spectra for Cu shown in Figure 4 are similar to those for Si in that the intensity of the simulated data differs from the experimental ones and that the surface loss features are more clearly more pronounced for 1000 eV. The width of the loss features agrees quite well in this case. Also, in the experimental data, a faint trace of the Cu MII edge at ~ 77 eV is discernable which is absent in the simulated data, being attributable to the fact that core-edges are difficult to describe by means of a Drude-Lindhard fit to optical data. The retrieved bulk loss distributions agree satisfactorily with theory, while the experimental surface loss distribution is slightly broader and tails off unexpectedly slowly towards higher loss energies. The larger width of the retrieved DSEP explains the higher intensity of the experimental raw data compared to the model calculations in Figure 4a, but the remaining intensity at loss energies above ~ 30 eV is not clear. It may be attributable to the uncertainty of the value of $\langle n_s \rangle$ used in the retrieval.

The results for Au are shown in Figure 5. Note that the shape of the raw data far away from the surface loss features is distinctly different for the two energies, as predicted by the corresponding sequences of bulk partial intensities for these energies, shown in Figure 2b. The retrieved loss distributions again agree quite well with theory except for deviations in the DIIMFP at around ~ 30 eV.

These deviations, however, are of the same order of magnitude as differences between different sets of optical data found in the literature, as shown in Figure 6. For Cu, the present data are in reasonable agreement with the DIIMFP calculated from optical data in Ref. [15] and Ref. [1], except for the two peaks at ~ 20 and ~ 30 eV which are slightly sharper as expected from the optical data. The density-functional-calculations of Ref. [40] agree closely with our data for the first peak at ~ 20 eV, but deviate for higher energies. For Au, on the basis of the good mutual consistency of the present data, and those of Ref. [15] and Ref. [1], one might be inclined to suspect a systematic error in the dataset of Ref. [41].

This comparison emphasizes the necessity of having an effective means for experimental determination of optical constants at one's disposal.

Since, in principle, optical data can be derived from experimental DIIMFPs, the present results are encouraging in that the proposed approach seems to open up a new way to obtain such data. The involved experimental procedure is conceivably straightforward and at any rate much simpler than other techniques to obtain optical data in this energy range like light scattering or loss measurements in the transmission microscope. Most importantly, data on the dielectric response can be derived from measurements with an inherent lateral resolution below a few nm on a specimen prepared in an arbitrary way (as long as it can be brought into an ultra-high vacuum chamber). This constitutes an important advantage over other measurements including loss measurements conducted in transmission.

A comparison as given here for Si, Cu and Au was made for other measured materials for which Drude–Lindhard parameters for the dielectric function have been published (Ag, Al, Be, Bi, C, Co, Fe, Ge, Mo, Ni, Pd, Pt, Ta, Te, Ti, V, W). These comparisons showed similar features as those for Si, Cu and Au, which therefore constitute a representative subset of all results.

For materials with sharp loss distributions the energy/angular dependence of the DIIMFP/DSEP produced spurious features in the retrieved data, as discussed for Si, and, in most cases, these were reproduced by the type III model calculations in much detail. For the other materials these deviations were smaller. Nonetheless it seems worthwhile to try to apply the proposed algorithm to angle resolved data (taken at the same energy) in order to reduce these spurious features. The remarkable agreement between the type III model calculations and experimental retrievals confirm the model of medium energy electron transport in solids in unprecedented detail (see Figure 3), in particular the angular dependence of the *shape* of the DSEP and the energy dependence of the *shape* of the DIIMFP, which are very subtle effects.

An issue that deserves to be addressed at this stage is the influence of an uncertainty in the input parameters on the outcome of the retrieval procedure. The input parameters comprise the elastic scattering cross section, and the total scattering probabilities, i.e. the inelastic mean free path and the surface excitation probability, or average number of surface excitations in a single surface crossing. While the scattering potential employed to establish the elastic cross section is known to critically affect the angular distribution of the elastic

peak intensity in some cases [42], it is not expected to affect the sequence of *reduced* partial intensities in a significant way since it is the *shape* of the pathlength distribution that governs the latter, while the absolute elastic peak intensity is determined by the absolute value of pathlength distribution [cf. Equation (9)]. The same reasoning holds for the inelastic mean free path that is used to convert the pathlength distribution into the sequence of partial intensities. These considerations are supported by the fact that the bulk loss distributions retrieved from experiment shown in Figs. 3–5 agree quite well –on an absolute scale– with the theoretical normalized DIIMFPs.

The relative error in the surface partial intensities is proportional to the relative error in the surface excitation parameter. the latter varies between ~ 1 – 2 for all materials studied so far and is known with an accuracy of about 10% [26]. Model calculations show that the main influence of an error in the SEP of this order of magnitude on the outcome of a retrieval is that the area under the retrieved curve deviates from unity by approximately the same relative amount. The deviations from theory observed for the DSEP of Cu can be explained in this way.

4. SUMMARY

The energy loss process of electrons reflected from solid surfaces was studied theoretically. It was shown that the Fourier transform of the loss spectrum can be written as a bivariate power series of the normalized differential surface and bulk loss distribution in individual collisions. A reversion of this bivariate power series is given on the basis of two input spectra with sufficiently different sequences of partial intensities. The resulting procedure was applied to model data and experimental spectra. The retrieved loss distributions compare satisfactorily with theory. On the whole, the results provide a detailed verification of the commonly accepted model of medium energy electron transport in solids. In particular, the energy/angular dependence of the *shape* of the DIIMFP and the DSEP was confirmed in detail for Si.

5. ACKNOWLEDGMENTS

The author is grateful to Dr. Claudia Ambrosch-Draxl for making the optical data of Ref. [40] available before publication and to Drs. Helmut Werner and Werner Smekal for fruitful discussions. Financial support of the present work by the Austrian Science Foundation FWF through Project No. P15938-N02 is gratefully acknowledged

- [1] E. D. Palik, *Handbook of optical constants of solids* (Academic Press, New York, 1985).
- [2] E. D. Palik, *Handbook of optical constants of solids II* (Academic Press, New York, 1991).
- [3] B. L. Henke, E. M. Gullikson, and J. C. Davis, *Atomic Data and Nuclear Data Tables* **54**, 181 (1993).
- [4] C. T. Chantler, *J. Phys. Chem. Ref. Data* **24**, 71 (1995).
- [5] C. T. Chantler, *J. Phys. Chem. Ref. Data* **29**, 597 (2000).
- [6] P. Schattschneider, *Fundamentals of Inelastic Electron Scattering* (Springer, New York, Vienna, 1986).
- [7] W. Kohn, *Rev. Mod. Phys.* **71**, 1253 (1999).
- [8] P. Blaha, K. Schwarz, G. K. H. Madsen, D. Kvasnica, and J. Luitz, *WIEN2k, an augmented plane wave and local orbitals program for calculating crystal properties* (TU Vienna, 2001).
- [9] W. S. M. Werner, *Surf Interface Anal* **31**, 141 (2001).
- [10] S. Tougaard and I. Chorkendorff, *Phys Rev* **B35**, 6570 (1987).
- [11] M. Vicanek, *Surf Sci* **440**, 1 (1999).
- [12] W. S. M. Werner, *Surf Interface Anal* **23**, 737 (1995).
- [13] W. Smekal, W. S. M. Werner, C. S. Fadley, and M. A. van Hove, *J Electron Spectrosc Rel Phen* **137**, 183 (2004).
- [14] A. Jablonski, F. Salvat, and C. J. Powell, *J. Phys. Chem. Ref. Data* **33**, 409 (2004).
- [15] C. J. Tung, Y. F. Chen, C. M. Kwei, and T. L. Chou, *Phys Rev* **B49**, 16684 (1994).
- [16] L. D. Landau and E. M. Lifshitz, *Theory of electromagnetism* (Pergamom Press, Oxford, New York, 1977), 3rd edition.
- [17] R. H. Ritchie, *Phys Rev* **106**, 874 (1957).
- [18] E. A. Stern and R. A. Ferrell, *Phys Rev* **120**, 130 (1960).

- [19] P. M. Echenique and J. B. Pendry, J. Phys. C: Solid State Phys **8**, 2936 (1975).
- [20] R. Nunez, P. M. Echenique, and R. H. Ritchie, J. Phys. C: Solid State Phys **13**, 4229 (1980).
- [21] F. Yubero and S. Tougaard, Phys Rev **B46**, 2486 (1992).
- [22] N. R. Arista, Phys Rev **A49**, 1885 (1994).
- [23] C. Denton, J. B. Gervasoni, R. O. Barrachina, and N. R. Arista, Phys Rev **A57**, 4498 (1998).
- [24] K. L. Aminov and J. B. Pedersen, Phys Rev **B63**, 125412 (2001).
- [25] S. Tanuma, C. J. Powell, and D. R. Penn, Surf Interface Anal **21**, 165 (1994).
- [26] W. S. M. Werner, W. Smekal, C. Tomastik, and H. Störi, Surf Sci **486**, L461 (2001).
- [27] W. S. M. Werner, Phys Rev (2005).
- [28] W. S. M. Werner, Phys Rev **B55**, 14925 (1997).
- [29] W. S. M. Werner, Surf Sci **526/3**, L159 (2003).
- [30] W. S. M. Werner, J. Zemek, and P. Jiricek, Phys Rev **B67**, 155412 (2003).
- [31] W. S. M. Werner, Surf Interface Anal **35**, 347 (2003).
- [32] W. S. M. Werner, H. Störi, and H. Winter, Surf Sci **518**, L569 (2002).
- [33] W. S. M. Werner and M. Hayek, Surf Interface Anal **22**, 79 (1994).
- [34] W. S. M. Werner, C. Tomastik, T. Cabela, G. Richter, and H. Störi, J Electron Spectrosc Rel Phen **113**, 127 (2001).
- [35] G. N. Raney, Trans AMS **94**, 441 (1960).
- [36] R. P. Brent and H. T. Kung, J Ass Comp Mach **25**, 581 (1978).
- [37] C. C. Cheng, J. H. McKay, J. Towber, S. S.-S. Wang, and D. L. Wright, Trans AMS **349**, 1769 (1997).
- [38] A. C. Yates, Comp Phys Comm **2**, 175 (1971).
- [39] R. A. Bonham and T. G. Strand, J Chem Phys **39**, 2200 (1963).
- [40] K. Glantschnig and C. Ambrosch-Draxl, Phys Rev (2005).
- [41] H. J. Hageman, W. Gudat, and C. Kunz, J. Opt. Soc. Am. **65**, 742 (1975).
- [42] C. J. Powell and A. Jablonski, J Phys Chem Ref Data **28**, 19 (1999).

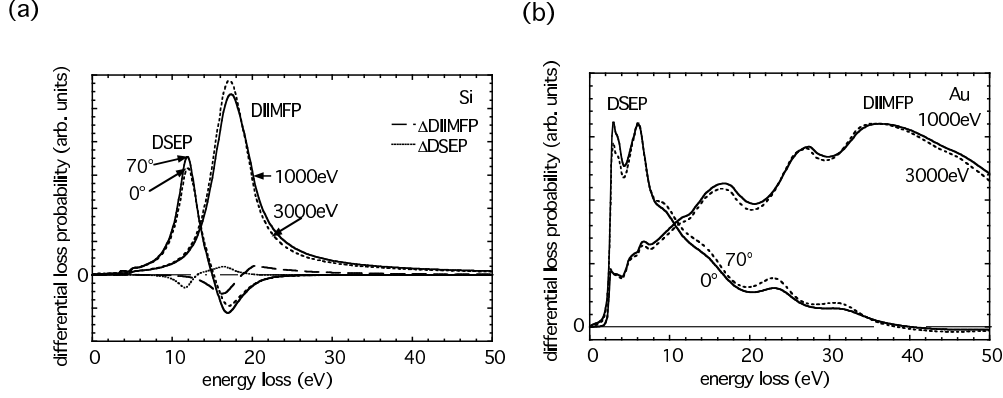


FIG. 1: Differential inverse inelastic mean free path (DIIMFP) and differential surface excitation probability (DSEP) for medium energy electrons in Si and Au. The DIIMFP is presented for 1000 eV (solid curves) and 3000 eV (dashed curves) while the DSEP is shown for 1000 eV for two different angles of surface crossing (0° , solid curves and 70° , dashed curves). The DSEP was divided by a factor of 5 to facilitate comparison. The curves labelled Δ DSEP and Δ DIIMFP in (a) represent the difference of the DSEP and DIIMFP for the considered angle of surface crossing and energy respectively. (a.) Si; (b.) Au.

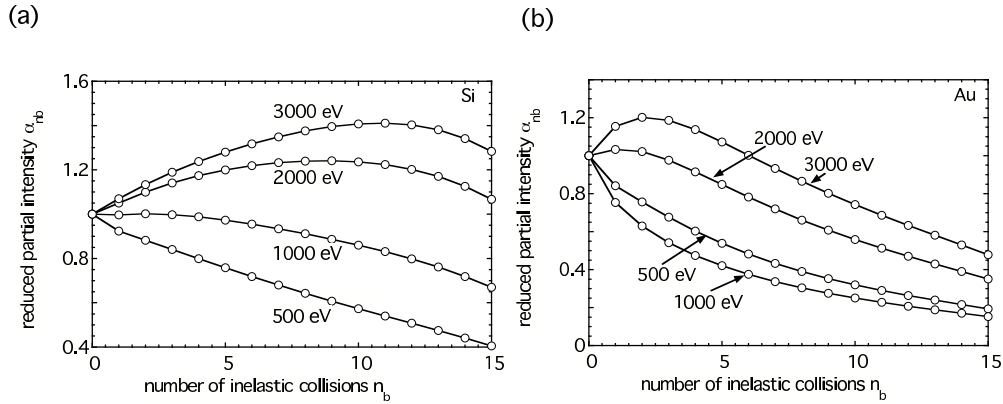


FIG. 2: Reduced partial intensities for quasi-elastic reflection, $\alpha_{n_b} = A_{n_b} / A_{n_b=0}$ for volume scattering for several energies. These model calculations were performed for normal incidence and for an off-normal emission direction of 60° (a.) Si; (b.) Au.

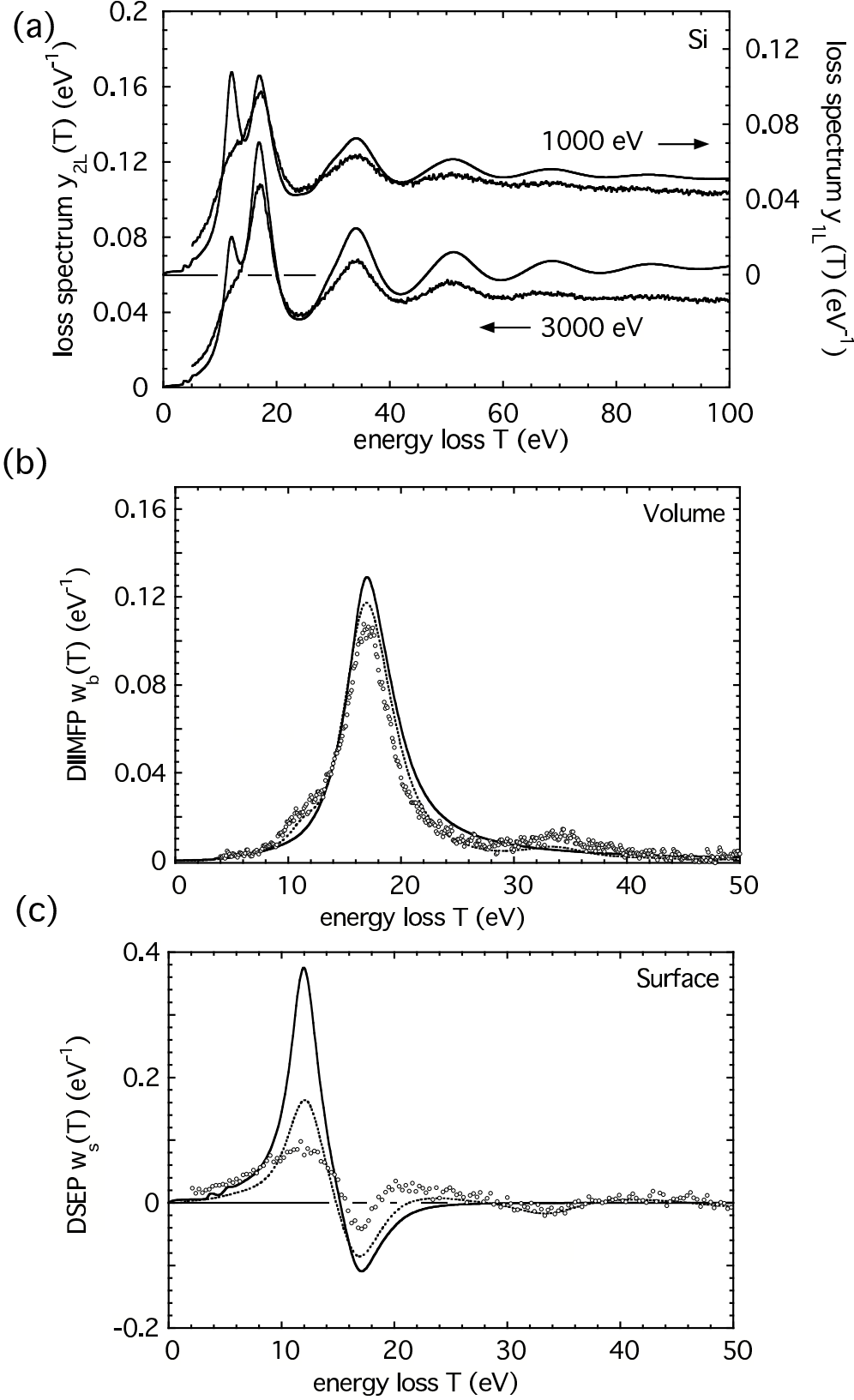


FIG. 3: (a.) Measured energy loss spectra for 1000 and 3000 eV for Si after removal of the elastic peak (noisy curves). The smooth curves are the simulated loss spectra using theoretical shapes for the DSEP and DIIMFP. (b.) Retrieved normalized DIIMFP (open circles). The solid curve is the theoretical result Equation (4). The dashed curve represents the retrieved volume loss distribution

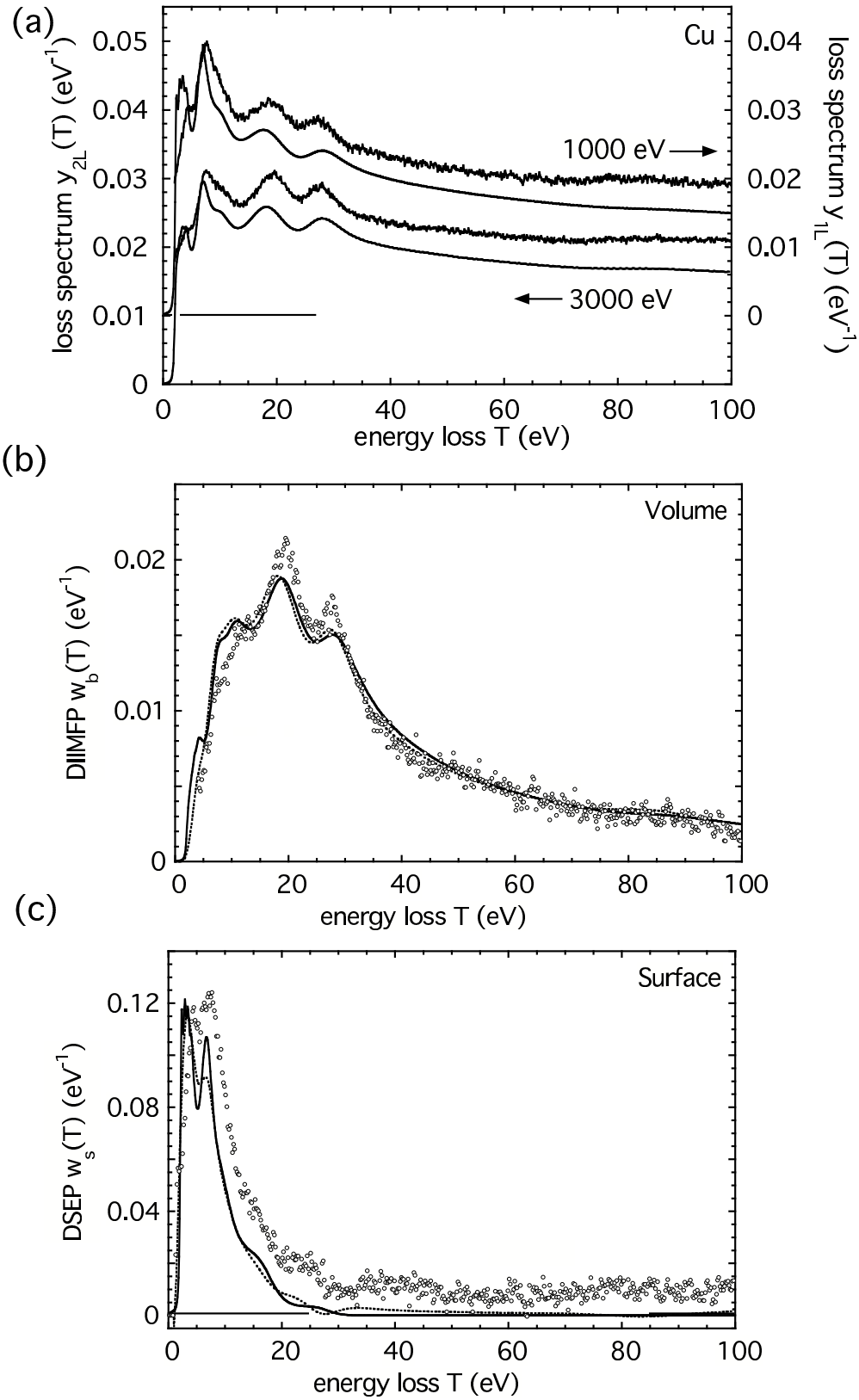


FIG. 4: Same as Figure 3 for Cu.

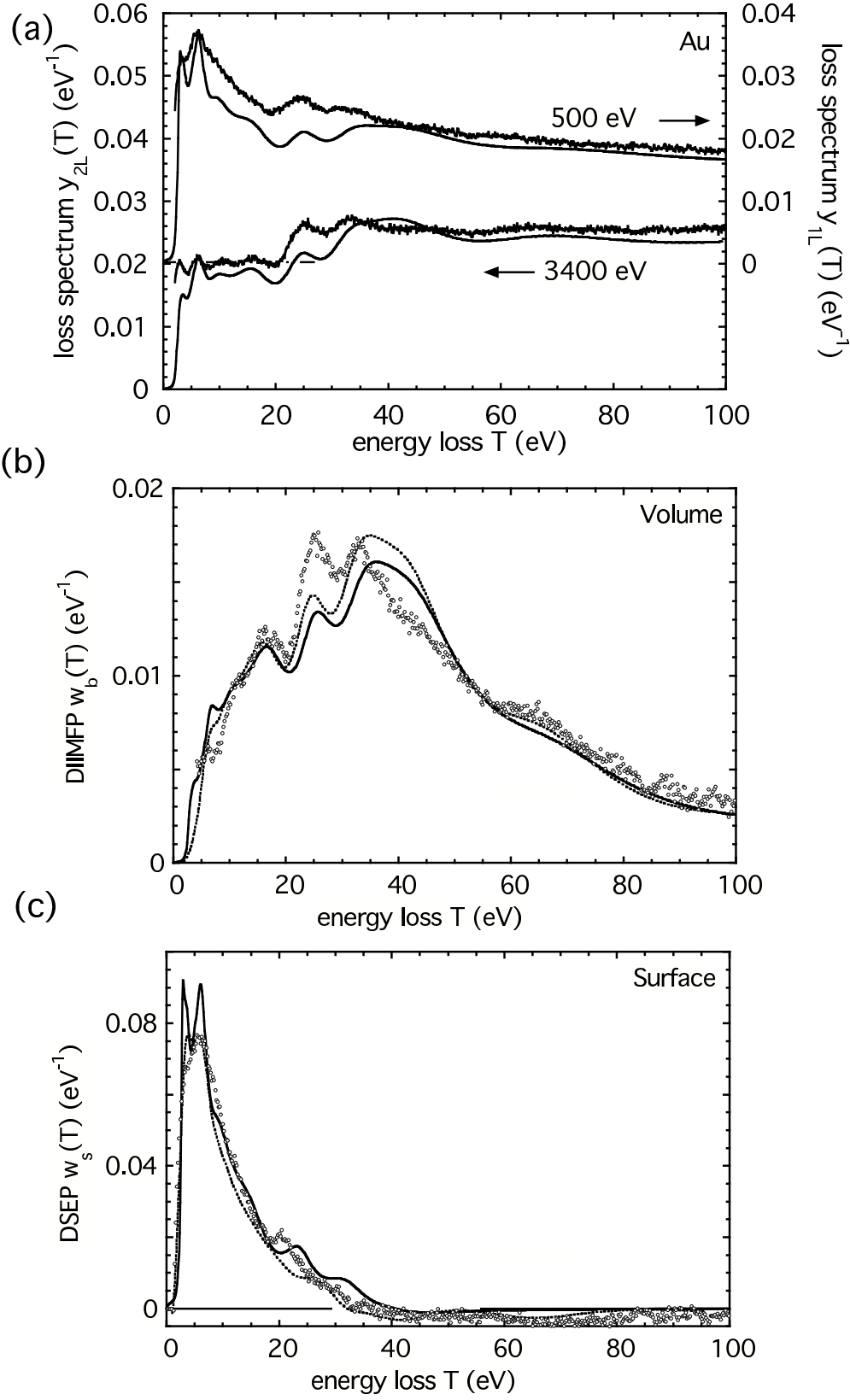
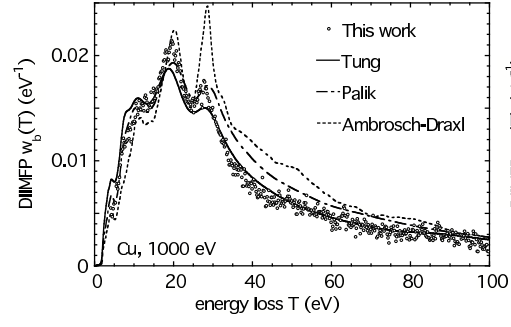


FIG. 5: Same as Figure 3 for Au for measured spectra taken at 500 and 3400 eV.

(a)



(b)

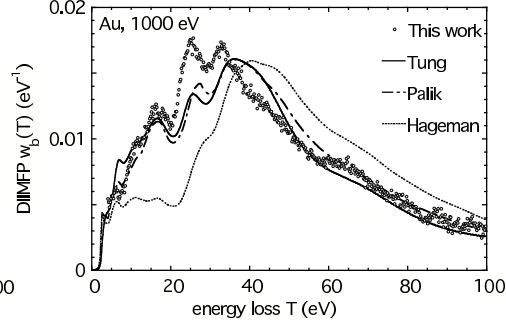


FIG. 6: Comparison of the DIIMFP obtained in the present work (open circles) with results based on Equation (1) using optical data taken from different sources. a.) Cu, 1000 eV. Solid curve: Tung, Ref. [15]; Dash dotted curve: Palik, Ref. [1]; Dotted curve: Ambrosch-Draxl, Ref. [40]; b.) Au, 1000 eV. Solid curve: Tung, Ref. [15]; Dash dotted curve: Palik, Ref. [1]; Dotted curve: Hageman, Ref. [41];